

# MUON SPIN ROTATION ANALYSIS OF THE INTERNAL MAGNETIC FIELD OF URANIUM BERYLLIUM 13

JACK LI

Uranium beryllium 13 ( $\text{UBe}_{13}$ ) is a heavy fermion system whose properties depend strongly on its internal magnetic structure. Different models have been proposed to explain its magnetic distribution, but additional experimental data is required. An experimental method that is particularly useful is muon spin spectroscopy ( $\mu\text{SR}$ ). In this process, positive muons are embedded into a sample where they localize at magnetically unique sites. The net magnetic field causes precession of the muon spin at the Larmor frequency, generating signals that can provide measurements of the internal field. This experiment specifically determines the muon localization sites of  $\text{UBe}_{13}$ . To do so, results from muon spin experiments at various temperatures and external magnetic field strengths are analyzed. The experiments took place at TRIUMF in the University of British Columbia. Data from the temperature and magnetic field ramps are analyzed through ROOT. The Fourier transforms of experimental data showed peaks of muon localization at the geometric centers of the edges of the crystal lattice. These results can be used to build a rigorous model of  $\text{UBe}_{13}$ 's internal magnetic structure and resulting magnetic field distribution.

## I. BACKGROUND

### A. Heavy Fermion Systems and Uranium Beryllium 13

Heavy fermions have been studied extensively and are the focus of modern physics research. These compounds are generally Ce, Yb, and U based intermetallics, although Np and Pu compounds are reported. A common feature among heavy fermion systems is the also the existence of a partially filled 4f or 5f electron shell. At room temperature, f-shell electrons remain at their atomic sites and the system behaves as an interacting collection of f-electron moments and conducting electrons. However, f-electron moments become coupled with conduction electrons and with each other at low temperatures. Thus, the effective mass of conduction electrons become 10 to 1000 times that of a bare electron. Many anomalies appear in heavy fermion systems at low enough temperatures.

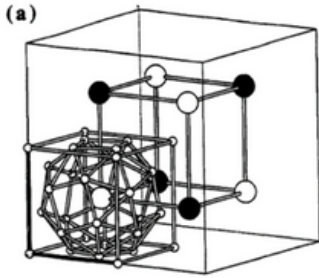


FIG. 1: Crystal structure of  $\text{UBe}_{13}$ .

Uranium beryllium 13 ( $\text{UBe}_{13}$ ) is a characteristic heavy fermion. The primary cube contains 8 uranium atoms, where 8 beryllium atoms form a cube around each uranium atom. 24 more beryllium atoms arrange themselves into a polyhedron structure inside the beryllium cube. Like most heavy fermion systems,  $\text{UBe}_{13}$  behaves

like a metal at room temperature. Chemical properties (e.g. resistivity, specific heat) change dramatically at 1-10 K, as if its outer-shell electrons were several orders of magnitude heavier. This behavioural shift can be explained by models that rely heavily on an understanding of the internal magnetic structure. There is still a lack of information on  $\text{UBe}_{13}$ , and this project aims to offer new insight to build a rigorous model of its internal magnetic structure.

Under the framework of muon spin spectroscopy ( $\mu\text{SR}$ ), this project determines the muon localization sites and takes advantage of the muon's strength as a magnetic probe to map its internal field distribution. The  $\mu\text{SR}$  process is discussed in more detail in the next section.

### B. $\mu\text{SR}$ Spectroscopy

$\mu\text{SR}$  is an abbreviation for muon spin spectroscopy and is a technique used in solid-state physics to probe the internal magnetic structures of various materials. The process generally involves three components: an experimental sample, a positive spin-polarized muon beam, and an exterior magnetic field  $\mathbf{B}_{\text{ext}}$ .

Positive muons are produced through a series of nuclear reactions and are collected to form a muon beam. The initial polarization of the muons in the beam is close to 100% i.e., the spin of the positive muons is opposite to the momentum. The muon beam is directed by electromagnetic field guides and shot into the sample being studied, where the muons are implanted at various interstitial sites inside the material. Locked in these sites, the muons spin at the Larmor frequency  $\omega_L$  related to the net magnetic field by  $\omega_L = \gamma_\mu |\mathbf{B}_{\text{net}}|$ , where  $\gamma_\mu$  is the known gyromagnetic ratio of the muon. This relationship can be determined theoretically, and the proof is given in section B of the Appendix.

While spinning, the muon undergoes a decay process, and the muon decays into a positron, a positron neutrino

and a muon anti-neutrino. The positron is emitted preferentially in the direction of the spin. The positrons can then be monitored and stored by detection electronics. In the case of this experiment, four positron detectors surround the sample. The four are named L(ef), R(ight), B(ack), F(orward).

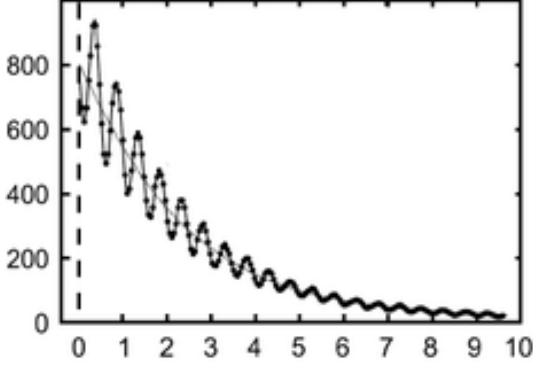


FIG. 2: An example of a positron counts versus time histogram. This experiment used four detectors in total, giving four of such graphs for each trial.

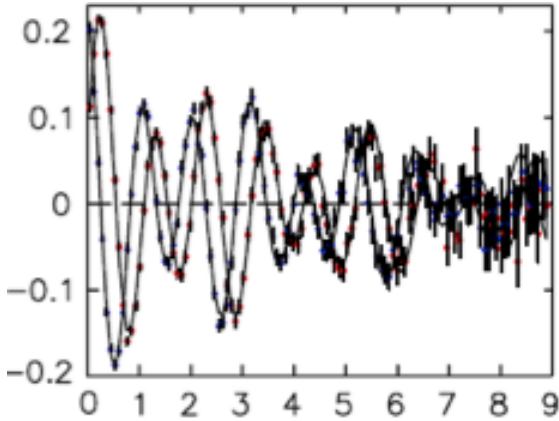


FIG. 3: Asymmetry vs time (given in microseconds) graph of two sets of opposing detectors on the same axes.

With this data, four histogram functions can be made for each detector -  $N_L(t)$ ,  $N_R(t)$ ,  $N_F(t)$  and  $N_B(t)$  (as in Figure 2). An additional set of functions, called the asymmetry functions, can be defined for each set of detectors:  $A_{BF}(t)$  and  $A_{LR}(t)$ . These can be written as the difference between the pairs of histograms divided by their sum.  $A_{BF}(t)$  can be expressed as

$$A_{BF}(t) = \frac{N_F(t) - N_B(t)}{N_F(t) + N_B(t)}$$

and  $A_{LR}(t)$  as

$$A_{LR}(t) = \frac{N_L(t) - N_R(t)}{N_L(t) + N_R(t)}.$$

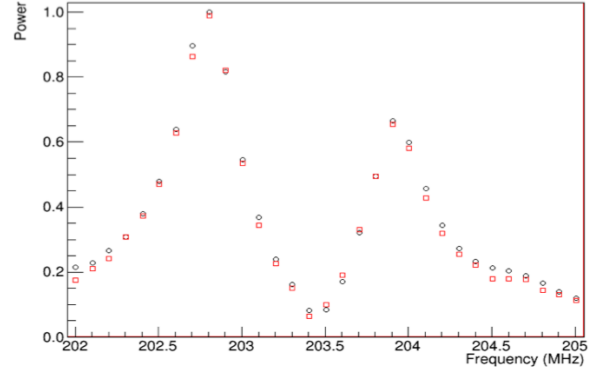


FIG. 4: Typical Fourier transform of an asymmetry function similar to the one in Figure 3. The peaks of this graph represent the most prominent muon Larmor frequencies that make up the corresponding asymmetry function.

Figure 3 gives a typical asymmetry function from a set of opposing detectors.

These two asymmetry functions can uncover details about the internal magnetic field. To do so, the Fourier transformation for the two asymmetry plots is taken for each trial. The peaks of the Fourier transforms give the most prominent frequencies of muon oscillation at interstitial sites, or specifically, the Larmor frequencies  $\omega_L$ .

The internal magnetic field of a crystal  $\mathbf{B}_{\text{int}}$  is related to the external magnetic field  $\mathbf{B}_{\text{ext}}$  and net magnetic field  $\mathbf{B}_{\text{net}}$  by the intuitive vector relationship

$$\mathbf{B}_{\text{net}} = \mathbf{B}_{\text{int}} + \mathbf{B}_{\text{ext}} \quad (1)$$

$\mathbf{B}_{\text{int}}$  can be deduced, as  $\mathbf{B}_{\text{ext}}$  is experimentally controlled and  $\mathbf{B}_{\text{net}}$  can be expressed in terms of the measured Larmor frequency.

## II. EXPERIMENTAL SETUP

Experiments took place on the M15 Beamline at TRIUMF, with a polarized  $\mu^+$  beam dedicated to the production of muons. The  $\text{UBe}_{13}$  crystals were oriented so that the magnetic field aligned with the [100] crystallographic direction, anti-parallel to the muon beam. Four positron detectors surrounded the sample.

The experiment was conducted so that two parameters were varied at a time: firstly, the temperature of the crystals. Table 1 gives the and secondly, the magnetic field surrounding the crystals. The experiment consisted of two data sweeps measuring the effect of each parameter while holding the other constant. Tables 1 describes the parameter variation for each series of measurements. The range of temperatures and magnetic field strengths are able to provide results from a variety of conditions.

The  $\text{UBe}_{13}$  crystals were located at the end of the beamline, under vacuum, and cooled by liquid nitrogen. The crystals were surrounded by a plastic scintillator,

Field (T)	1.5	1.5	1.5	1.5	1.5	1.5
Temperature (K)	275	200	125	75	25	3

---

Field (T)	0.5	0.75	1.0	1.5	2.0	2.5
Temperature (K)	3	3	3	3	3	3

TABLE I: Top gives the temperature change with constant field. Bottom gives the magnetic field change with constant temperature.

which generated photons when struck by decay positrons. The photons traveled through a light guide to a photomultiplier, generating an electrical pulse to the surrounding positron detectors. Scintillators on opposite sides of the crystal then produced an anisotropic signal that oscillates with muon decay. Two additional scintillators were in the beam-line to track the muons. These scintillators were made of plastic, and had a thickness of approximately 0.25 mm that allowed muons to pass through while being counted. The first scintillator was placed in the beamline before the crystals, and the second located just before the  $\text{UBe}_{13}$  crystals. Muon localization in the sample depended on the intensity of the muon beam at the sample. A superconducting solenoid called Helios was used to apply a large magnetic field to the sample. The Helios controlled the width of the beamline close to the sample, and limited the number of muons impinging on the  $\text{UBe}_{13}$  crystals. The goal was to detect 1 muon every 10  $\mu\text{s}$ . If two muons were stopped within that time interval, the measurement was discarded to ensure that an emitted positron could be correctly matched to a single implanted muon.

The  $\text{UBe}_{13}$  sample was cooled to extremely low temperatures. Such cooling was made possible by liquid helium cooling and the length of the shaft that the crystals were mounted on. The difference in temperature between the end of the shaft and the sample resulted in a large temperature gradient. The temperatures were controlled by both the liquid helium cooling system and an automatic heater. The sample was cooled slightly below the desired temperature so that the heater could fine-tune the samples to the desired temperature within an acceptable range of fluctuation. Data was analyzed using ROOT developed by the European Council for Nuclear Research (CERN).

### III. RESULTS AND DISCUSSION

This section focuses on the determination of these muon localization sites. The anisotropy of detection events measured in the experiment correspond to the Larmor frequencies of muons localized in the sample. This can as a result give a measurement of the time averaged net magnetic field felt by the muons. Results show several important properties of  $\text{UBe}_{13}$ .

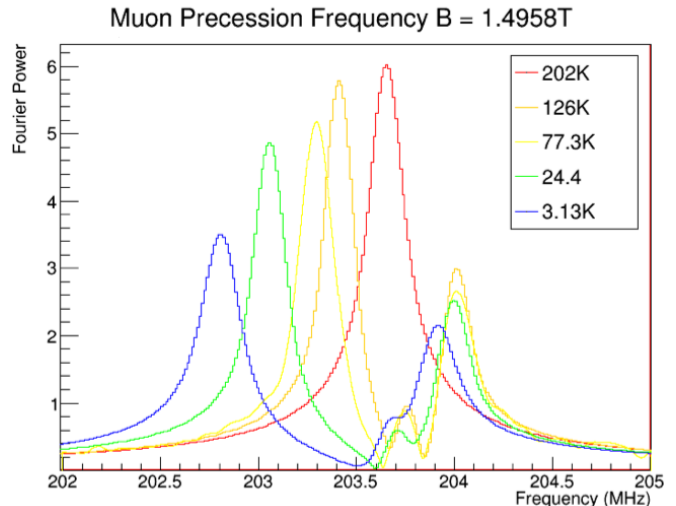


FIG. 5: The Fourier transform of the asymmetry data for 5 temperatures all at the same magnetic field of 1.5 T. At some temperature between 202 K and 126 K, muons are able to localize within the lattice, shown by the Larmor frequency splitting. The smaller peaks on the right represent the parallel interstitial lattice positions while the larger peaks on the left represent the perpendicular positions. Parallel lattice positions remain unaffected by the temperature change, while perpendicular positions are affected greatly.

From the Fourier transform of asymmetry data of each trial, runs for high temperatures ( $> 150$  K) gave a single peak Larmor frequency as seen in Figure 5. The reason for this is that the muons at these temperatures possess high amounts of thermal energy, and cannot be localized to any particular spot in the material lattice. Muons instead possess enough thermal energy to move between lattice sites and through the crystal. The result is a distribution of Larmor frequencies for muons propagating through the lattice. Additionally, thermal fluctuations within  $\text{UBe}_{13}$  can distort some of the net magnetization induced by the externally applied magnetic field. For both these reasons, the results indicate a single peak corresponding to the average Larmor frequency of all muons in all lattice spots (as in the 202 K case in Figure 6).

As temperature is lowered below the mobility limit, two distinct peaks begin to appear, as seen in Figure 5. As mentioned earlier, the dual peaks may be a result of the result of muons coming to rest at two magnetically unique crystal lattice sites. Observing all possible muon sites, the most plausible locations are described in Figure 6. These sites can correspond to either site I, in which the edge it is resting on is perpendicular to the external field, or site II, where the edge is parallel with the external field. The orientations of the dipole moments cause two magnetically unique sites at I and II. As the ratio between the magnitude of the two peaks for each temperature in the Fourier transform (Figure 5) is approximately 2:1, this provides evidence for the existence of multiple localization sites; there are 8 perpendicular sites (like in

I) and 4 parallel sites (as in II), which form a similar 2:1 ratio. The frequency splitting can thus be attributed to the magnetic environments of the parallel and perpendicular muon sites, the higher peak corresponding to the muon Larmor frequency at the perpendicular sites and the lower peak to that at the parallel sites.

Another possible localization site seen in other uranium based crystals is at the geometric center of the lattice – results do not support this however. If muon localization does occur at this central site, an additional third peak would have been traced in the Fourier transform. As there are two well-defined peaks and that localization at site I implies localization at site II (and vice versa) due to crystal symmetry, there is no evidence that the geometric center serves as a muon site.

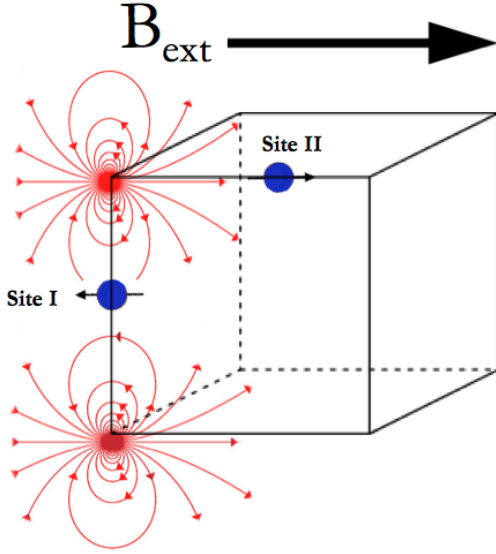


FIG. 6: I and II are possible localization sites for implanted muons in the  $\text{UBe}_{13}$  crystal, represented by blue spheres. Red spheres represent uranium atoms with their dipole fields aligned with  $\mathbf{B}_{\text{ext}}$ . Note there are 8 muon sites perpendicular to the magnetic field (symmetrical to I) and 4 parallel to the field (symmetrical to II). Beryllium atoms are not shown for simplicity.

Identifying the muon sites of  $\text{UBe}_{13}$  can allow for the calculation of the internal magnetic field  $\mathbf{B}_{\text{int}}$  from Equation 1:  $\mathbf{B}_{\text{net}} = \mathbf{B}_{\text{int}} + \mathbf{B}_{\text{ext}}$ . In the presence of an external magnetic field  $\mathbf{B}_{\text{ext}}$ , the muon spins at their lattice sites align parallel with  $\mathbf{B}_{\text{ext}}$  (see sites I and II from Figure 6). Assuming perfect muon spin alignment with  $\mathbf{B}_{\text{ext}}$ , tracing these magnetic dipole lines reveal that the magnetic field at the various lattice sites  $\mathbf{B}_{\text{int}}$  is directly parallel with the external field.

From Section 1.2, the Larmor frequency  $\omega_L$  equals  $\gamma_\mu |\mathbf{B}_{\text{net}}|$ , where  $\gamma_\mu$  is the gyromagnetic ratio. Thus,  $|\mathbf{B}_{\text{net}}|$  is equivalent to  $\frac{\omega_L}{\gamma_\mu}$ . From Equation 5, an expression for the internal field is simply  $\mathbf{B}_{\text{int}} = \frac{\omega_L}{\gamma_\mu} \mathbf{j} - \mathbf{B}_{\text{ext}}$  or in terms of linear frequency

$$\mathbf{B}_{\text{int}} = \frac{2\pi}{\gamma_\mu} f_L \cdot \mathbf{j} - \mathbf{B}_{\text{ext}} \quad (2)$$

where  $\mathbf{j}$  is the unit vector in the same direction as  $\mathbf{B}_{\text{int}}$  and  $\mathbf{B}_{\text{ext}}$ .

Fit results for the **temperature ramp** are listed below. Table II gives results for the perpendicular sites, while Table III gives results for the parallel sites. The calculated magnitude of the internal magnetic fields are given as well.

$\mathbf{B}_{\text{ext}}$ (T)	Temp. (K)	$f_{L\perp}$ (MHz)	$\mathbf{B}_{\text{int}\perp}$ (T)
1.4958	3	202.8113	$5.3370 \times 10^{-4}$
1.4958	25	203.0593	$2.3632 \times 10^{-3}$
1.4958	75	203.3027	$4.1587 \times 10^{-3}$
1.4958	125	203.4158	$4.9940 \times 10^{-3}$
1.4958	200	203.6529	$6.7430 \times 10^{-3}$

TABLE II: External magnetic field  $|\mathbf{B}_{\text{ext}}|$  and Larmor frequency  $f_{L\perp}$  data for the perpendicular lattice sites during the temperature ramp. The magnitude of the internal magnetic field  $|\mathbf{B}_{\text{int}\perp}|$  is calculated.

$\mathbf{B}_{\text{ext}}$ (T)	Temp. (K)	$f_{L\parallel}$ (MHz)	$\mathbf{B}_{\text{int}\parallel}$ (T)
1.4958	3	203.9058	$9.4088 \times 10^{-3}$
1.4958	25	203.9863	$1.0000 \times 10^{-2}$
1.4958	75	204.0007	$1.0109 \times 10^{-2}$
1.4958	125	204.0010	$1.0111 \times 10^{-2}$
1.4958	200	203.6529	$6.7430 \times 10^{-3}$

TABLE III: External magnetic field  $|\mathbf{B}_{\text{ext}}|$  and Larmor frequency  $f_{L\parallel}$  data for the parallel lattice sites during the temperature ramp. The magnitude of the internal magnetic field  $|\mathbf{B}_{\text{int}\parallel}|$  is calculated.

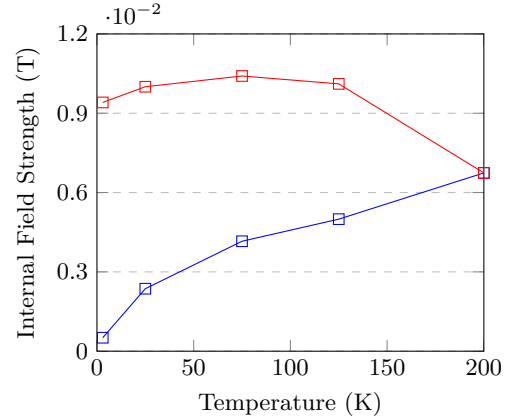


FIG. 7: The internal field strengths plotted against temperature. Data is from the temperature ramp. The blue curve denotes  $\mathbf{B}_{\text{int}\perp}$  and the red curve denotes  $\mathbf{B}_{\text{int}\parallel}$ .

Fit results for the **magnetic field ramp** are listed below. Table IV gives results for the perpendicular sites, while Table V gives results for the parallel sites. The calculated magnitudes of the internal magnetic fields are given as well.

$\mathbf{B}_{\text{ext}}$ (T)	Temp. (K)	$f_{L\perp}$ (MHz)	$\mathbf{B}_{\text{int}\perp}$ (T)
0.50	3.061	67.6263	$-1.0558 \times 10^{-3}$
0.75	3.125	101.4496	$-1.5109 \times 10^{-3}$
1.00	3.160	135.2578	$-2.0736 \times 10^{-3}$
1.50	3.110	202.7998	$-3.7511 \times 10^{-3}$
2.00	3.135	270.4000	$-5.0000 \times 10^{-3}$
2.50	3.149	337.9396	$-6.6950 \times 10^{-3}$
3.00	3.181	405.4530	$-8.5839 \times 10^{-3}$

TABLE IV: External magnetic field  $|\mathbf{B}_{\text{ext}}|$  and Larmor frequency  $f_{L\parallel}$  data for the parallel lattice sites during the magnetic field ramp. The magnitude of the internal magnetic field  $|\mathbf{B}_{\text{int}\perp}|$  is calculated.

$\mathbf{B}_{\text{ext}}$ (T)	Temp. (K)	$f_{L\parallel}$ (MHz)	$\mathbf{B}_{\text{int}\parallel}$ (T)
0.5	3.061	67.9974	$1.6821 \times 10^{-3}$
0.75	3.125	102.0027	$2.5719 \times 10^{-3}$
1.00	3.160	135.9950	$3.3657 \times 10^{-3}$
1.50	3.110	203.9092	$4.4433 \times 10^{-3}$
2.00	3.135	271.8340	$5.5804 \times 10^{-3}$
2.50	3.149	339.762	$6.7505 \times 10^{-3}$
3.00	3.181	407.6690	$7.7766 \times 10^{-3}$

TABLE V: External magnetic field  $|\mathbf{B}_{\text{ext}}|$  and Larmor frequency  $f_{L\parallel}$  data for the parallel lattice sites during the magnetic field ramp. The magnitude of the internal magnetic field  $|\mathbf{B}_{\text{int}\parallel}|$  is calculated.

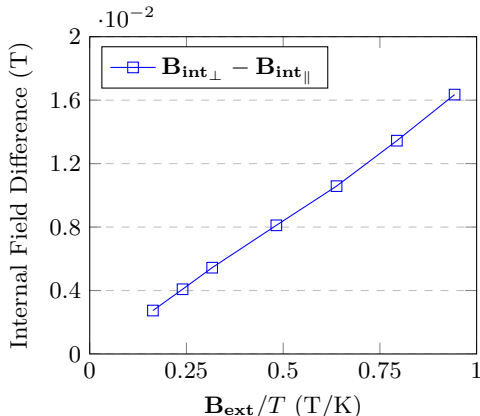


FIG. 8:  $\mathbf{B}_{\text{int}\perp} - \mathbf{B}_{\text{int}\parallel}$  vs.  $\mathbf{B}_{\text{ext}}/T$ , where  $T$  denotes the temperature of the sample. Data is taken from the magnetic field ramp. An interesting note from Curie's Law is that magnetization is proportional to  $\mathbf{B}_{\text{ext}}/T$ .

An interesting note from these results is that the internal field at perpendicular sites is anti-parallel to the externally applied field at low temperatures and weak magnetic field strengths, as shown in Table IV. Looking at the superposition of magnetic dipole moments of uranium atoms can reveal the reasons behind this. As shown in Figure 6, the magnetic dipole moments superimpose each other in the opposite direction of  $\mathbf{B}_{\text{ext}}$  at the perpendicular lattice sites (at Site I).

A contesting theory attempting to explain the magnetic structure of  $\text{UBe}_{13}$  is based on the concept of the

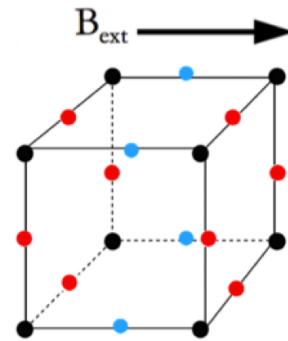


FIG. 9: Map of the internal magnetic field of  $\text{UBe}_{13}$  at its muon localization sites. Red spots are weaker magnetic sites and blue spots are stronger magnetic sites.

polaron. Polarons are quasiparticles – they are not a physical particles but interactions between electrons (or muons) with atoms in crystals. Polarons are induced in  $\text{UBe}_{13}$  by the introduction of muons in the crystal sample. As muons are negatively charged, they attract positive ions and repel negative ions, causing a temporary region of asymmetry. This region is the polaron, which can then diffuse through the crystal. The polaron has the ability to change the orientation of the magnetic dipole moments of surrounding magnetic ions - uranium ions in this case. The polaron can align these dipole moments, causing a larger magnetic moment and a greater internal field as a result.

Results of this experiment do not support the existence of magnetic polarons. If polarons did appear, frequency distributions seen in Figure 5 would reveal approximately equal distributions between the frequencies, given the random nature of the polaron's movement. The 2:1 ratio as seen from the experiment does not agree with this theory.

#### IV. SUMMARY AND CONCLUSION

The experiment examined the internal magnetic structure of  $\text{UBe}_{13}$  using  $\mu\text{SR}$  at TRIUMF. The data reveals two primary Larmor frequencies consistent with muons occupying magnetically unique lattice sites that are parallel and perpendicular to the external field. The Fourier power of the two peaks correspond roughly to the expected distribution in muon stopping sites. At temperatures higher than the mobility limit, thermal energy causes the muon to travel between muon sites, forming a single peak. However at lower temperatures, such thermal energy was removed and the oscillation between lattice locations decreased, forming two distinct peaks in the spectrum. Increased field splitting between sites at higher levels of magnetization could also verify the location of these muon stopping sites. The applied magnetic field was used to induce a net magnetization in the  $\text{UBe}_{13}$  sample, which allowed for sensitive inter lattice measure-



ments.

UBe<sub>13</sub> has a cubic structure and is therefore one of the most straightforward heavy fermions to study. As a characteristic heavy fermion, UBe<sub>13</sub>'s magnetic properties can readily be applied to other heavy fermion systems. Although applications of UBe<sub>13</sub> are not known as of yet, recent years have seen the identification of quantum critical points in a host of antiferromagnetic heavy-fermion compounds. The ability to harness the behaviors of heavy fermions could lead to rapid development in quantum computers and new generations of technology.

## V. ACKNOWLEDGEMENTS

The author would like to thank Eric Woolsey for his mentorship during this project. He would also like to thank Prof. Andrew MacFarlane and Prof. Robert Kiefl for their openness to discussion and helpful comments during the course of writing.

### Appendix A: Error Tables

Error analysis can be done via error propagation, and the uncertainty of the calculated values of  $\mathbf{B}_{\text{int}}$ ,  $\delta\mathbf{B}_{\text{int}}$ , can be found with the formula

$$\delta\mathbf{B}_{\text{int}} = \sqrt{\left(\frac{2\pi}{\gamma_{\mu}} \cdot \delta f_L\right)^2 + (\delta\mathbf{B}_{\text{ext}})^2} \quad (\text{A1})$$

where  $\delta f$  denotes the error of the measured Larmor frequency and  $\delta\mathbf{B}_{\text{ext}}$  the error of the controlled external magnetic field.  $\delta\mathbf{B}_{\text{ext}}$  is given to be at most  $10^{-5}$  T. The calculated values of  $\delta\mathbf{B}_{\text{int}}$  are thus higher approximations of the actual magnitudes of error.

Tables VI and VII below give  $\delta\mathbf{B}_{\text{int}\perp}$  and  $\delta\mathbf{B}_{\text{int}\parallel}$  for the **temperature ramp**.

$\mathbf{B}_{\text{ext}}$ (T)	Temp. (K)	$\delta f_{L\perp}$ (MHz)	$\delta\mathbf{B}_{\text{int}\perp}$ (T)
1.4958	3	0.0016	$1.5471 \times 10^{-5}$
1.4958	25	0.00094	$1.21696 \times 10^{-5}$
1.4958	75	0.00082	$1.16877 \times 10^{-5}$
1.4958	125	0.00076	$1.14648 \times 10^{-5}$
1.4958	200	0.0010	$1.24272 \times 10^{-5}$

TABLE VI: Magnitudes of the error of the calculated values of  $\mathbf{B}_{\text{int}}$  at the perpendicular sites for the temperature ramp.

$\mathbf{B}_{\text{ext}}$ (T)	Temp. (K)	$\delta f_{L\parallel}$ (MHz)	$\delta\mathbf{B}_{\text{int}\parallel}$ (T)
1.4958	3	0.0015	$1.4916 \times 10^{-5}$
1.4958	25	0.0018	$1.6624 \times 10^{-5}$
1.4958	75	0.0019	$1.7219 \times 10^{-5}$
1.4958	125	0.0016	$1.5471 \times 10^{-5}$

TABLE VII: Magnitudes of the error of the calculated values of  $\mathbf{B}_{\text{int}}$  at the parallel sites for the temperature ramp

Tables VIII and IX give  $\delta\mathbf{B}_{\text{int}\perp}$  and  $\delta\mathbf{B}_{\text{int}\parallel}$  for the **magnetic field ramp**.

$\mathbf{B}_{\text{ext}}$ (T)	Temp. (K)	$\delta f_{L\perp}$ (MHz)	$\delta\mathbf{B}_{\text{int}\perp}$ (T)
0.5	3.061	0.00070	$1.12549 \times 10^{-5}$
0.75	3.125	0.0010	$1.47898 \times 10^{-4}$
1	3.160	0.0109	$8.10391 \times 10^{-5}$
1.5	3.110	0.0019	$1.72194 \times 10^{-5}$
2	3.135	17.44	$1.28376 \times 10^{-1}$
2.5	3.149	2.81	$2.0658 \times 10^{-2}$
3	3.181	0.0460	$3.53812 \times 10^{-5}$

TABLE VIII: Magnitudes of the error of the calculated values of  $\mathbf{B}_{\text{int}}$  at the perpendicular sites for the magnetic field ramp.

$\mathbf{B}_{\text{ext}}$ (T)	Temp. (K)	$\delta f_{L\parallel}$ (MHz)	$\delta\mathbf{B}_{\text{int}\parallel}$ (T)
0.5	3.061	0.0010	$1.24272 \times 10^{-5}$
0.75	3.125	0.0015	$1.24272 \times 10^{-5}$
1	3.160	0.0046	$3.53812 \times 10^{-5}$
1.5	3.110	0.0020	$1.78252 \times 10^{-5}$
2	3.135	0.0032	$2.56600 \times 10^{-1}$
2.5	3.149	0.013	$9.64334 \times 10^{-2}$
3	3.181	4.12	$2.95117 \times 10^{-2}$

TABLE IX: Magnitudes of the error of the calculated values of  $\mathbf{B}_{\text{int}}$  at the parallel sites for the magnetic field ramp.

### Appendix B: Derivation of the Larmor Frequency

A particle in a quantum system is represented by a wave function

$$\psi(\mathbf{x}, t, \mathbf{s})$$

where  $\psi^2(\mathbf{x}, t, \mathbf{s})$  determines the probability of finding a particle with spin  $\mathbf{s}$  at position  $\mathbf{x}$  at time  $t$ . In some cases, the wavefunction  $\psi(\mathbf{x}, t, \mathbf{s})$  can be written in the form  $\phi(\mathbf{x}, t) \theta(\mathbf{s}, t)$ , where the  $\phi$  component is called the *position state* and  $\theta$  is called the *spin state*. The discussion hereon focuses on this spin factor. A common way of expressing the spin state is through bra-ket notation, denoted by the "ket" vector  $|\theta\rangle$ . As the rest of this paper deals exclusively with fermions, which has only two spin states ( $\pm\frac{1}{2}$ ),  $|\theta\rangle$  can be expressed as a linear combination of the  $+\frac{1}{2}$  state  $|+\rangle$  and the  $-\frac{1}{2}$  state  $|-\rangle$ . These two states can also be written as column vectors, with

$$|+\rangle = \begin{bmatrix} 1 \\ 0 \end{bmatrix}, |-\rangle = \begin{bmatrix} 0 \\ 1 \end{bmatrix}$$

meaning that for the general spin state,

$$|\theta\rangle = \begin{bmatrix} a \\ b \end{bmatrix}$$

where  $a$  and  $b$  are numerical values with the restriction that  $a^2 + b^2 = 1$ . Measurable quantities such as position,

velocity, angular momentum are represented by a corresponding operator. Operators act on wavefunctions to produce defined quantities. In special cases, the result of such an operation can be written as

$$O|\theta\rangle = \lambda|\theta\rangle$$

where  $O$  is the operator with the original wavefunction  $|\theta\rangle$ . If this case were to arise, the wavefunction  $|\theta\rangle$  is an *eigenfunction* of  $O$  with a scaling factor  $\lambda$ , called an *eigenvalue*. Then, the eigenvalue  $\lambda$  will be observed if a measurement of the observable operator  $O$  is made on the state  $\theta$ . In vector form, operators are in some cases  $2 \times 2$  matrices.

A special type of operator is the Hamiltonian, which corresponds to the observable that is the system's *energy*. The *Zeeman interaction*, the energy between the magnetic moment and the applied magnetic field, is a Hamiltonian and is perhaps the most important interaction in magnetic resonance. The Zeeman interaction written as a  $2 \times 2$  matrix is:

$$\mathcal{H} = -\frac{\hbar\gamma_\mu B}{2} \begin{bmatrix} 1 & 0 \\ 0 & -1 \end{bmatrix} \quad (\text{B1})$$

where  $B$  is the exterior magnetic field.

A particle's state at any time can be found by using the time evolution operator, defined as

$$U(t) = \exp \frac{-i\mathcal{H}t}{\hbar}.$$

Via Equation B1 and Taylor expansion of  $e^x$ , the operator can be written as a  $2 \times 2$  matrix as

$$U(t) = \begin{bmatrix} \exp \frac{i\gamma_\mu Bt}{2} & 0 \\ 0 & \exp \frac{i\gamma_\mu Bt}{2} \end{bmatrix}$$

Thus, calling a state at time  $t = 0$

$$|\psi(0)\rangle = \begin{bmatrix} a \\ b \end{bmatrix}$$

where  $a$  and  $b$  are numerical values such that  $a^2 + b^2 = 1$ , the time evolution operator  $U(t)$  can be used to give the state at any later time  $t$ :

$$|\psi(t)\rangle = \begin{bmatrix} \exp \frac{i\gamma_\mu Bt}{2} & 0 \\ 0 & \exp \frac{i\gamma_\mu Bt}{2} \end{bmatrix} \begin{bmatrix} a \\ b \end{bmatrix} = \begin{bmatrix} a \\ b \end{bmatrix} e^{i\gamma_\mu Bt} \quad (\text{B2})$$

Equation B2 can be written as a trigonometric expression via Euler's formula. The periodic motion of the muon is given an associated value  $\omega_L = \gamma_\mu B$ , the *Larmor frequency*.

- 
- [1] S. Sakarya, Magnetic Properties of Uranium Based Ferromagnetic Superconductors, thesis, (2007).
  - [2] C. Lin, Microwave Surface Impedance Measurements. (1999)
  - [3] A. L. Yaouanc and D. R. Pierre, Muon Spin Rotation, Relaxation, and Resonance: Applications to Condensed Matter, (2010).
  - [4] J. Jang, T. Uittenbosch, E. Woolsey, N. Zacchia, Analysis of the Internal Magnetic Field of  $\text{UBe}_{13}$ , (2016).
  - [5] R.H. Heffner, D.W. Cooke, Z. Fisk, R.L. Hutson, M.E. Schillaci, J.L. Smith, J.O. Willis, D.E. Maclaughlin, C. Boekema, R.L. Lichti, A.B. Denison, and J. Oostens, Muon Knight shift and zero-field relaxation in  $(\text{U,Th})\text{Be}_{13}$  (1986).
  - [6] J. L. Smith, Z. Fisk, J. O. Willis, B. Batlogg, & H. R. Ott. Impurities in the heavy fermion superconductor  $\text{UBe}_{13}$ . (1984)
  - [7] A. Ramirez, P. Chandra, P. Coleman, Z. Fisk, J. Smith, and H. Ott, Physical review letters 73, 3018 (1994).
  - [8] J. Flouquet, G. Knebel, D. Braithwaite, D. Aoki, J.-P. Brison, F. Hardy, A. Huxley, S. Raymond, B. Salce, and I. Sheikin, Comptes Rendus Physique 7, 22 (2006).
  - [9] M. Liu, Properties of Heavy Fermion Systems, (2010).
  - [10] A. MacFarlane, Introduction To Magnetic Resonance Probes Of Materials. 1st ed. (2017).
  - [11] V. Storchak, J. Brewer, D. Eshchenko, P. Mengyan, O.

Parfenov, A. Tokmachev, P. Dosanjh, Z. Fisk, and J. Smith, New Journal of Physics 18, 083029 (2016).

JACK LI, ST. GEORGE'S SCHOOL, 4175 W 29TH AVE, VANCOUVER, BC V6S 1V1, CANADA

E-mail address, jackli6410@gmail.com